NACA

RESEARCH MEMORANDUM

WING-BODY COMBINATIONS WITH WINGS OF VERY LOW

ASPECT RATIO AT SUPERSONIC SPEEDS

By Leland H. Jorgensen and Elliott D. Katzen

Ames Aeronautical Laboratory
Moffett Field, Calif.

NATIONAL ADVISORY COMMITTEE
FOR AERONAUTICS
WASHINGTON
October 26, 1956

NATIONAL ADVISORY COMMITTEE FOR AERONAUTICS

RESEARCH MEMORANDUM

WING-BODY COMBINATIONS WITH WINGS OF VERY LOW

ASPECT RATIO AT SUPERSONIC SPEEDS

By Leland H. Jorgensen and Elliott D. Katzen

SUMMARY

Force and moment characteristics of configurations employing wings of very low aspect ratio (1 and less) have been determined for Mach numbers of 1.97 and 3.33. The angle-of-attack range was from 0° to 17° for Mach number 1.97 and from 0° to 30° for Mach number 3.33. The Reynolds number was about 9×10^6, based on body length.

The results of this investigation indicate that there are distinct aerodynamic advantages to the use of highly swept wings of very low aspect ratio. Some of these advantages are high lift effectiveness, compared to that of wingless missiles, and little drag penalty with shapes that appear to be beneficial for decreasing aerodynamic heating. These low-aspect-ratio configurations exhibit small center-of-pressure shifts and small rolling moments with changes in angle of attack and Mach number; therefore, stability and control problems are simplified.

Comparisons of theoretical and experimental force and moment characteristics indicate that existing wing-body interference theory is not generally adequate for missile configurations employing wings of very low aspect ratio.

INTRODUCTION

Results of development tests and studies made by various aircraft companies have shown that for certain applications, missiles employing wings of very low aspect ratio have excellent aerodynamic characteristics. In other studies attention has been focused on the possible use of wings of very low aspect ratio by questioning the desirability and need for wings of large span. There are, however, many gaps in our knowledge concerning the aerodynamics of missiles having wings of very low aspect ratio. To help provide some of the required information, an experimental investigation of the aerodynamic characteristics of a family of missile-like configurations has been made. A brief discussion of the results of this investigation was presented in reference 1. The

principal purpose of the present report is to supplement reference 1 with a discussion of much of the data previously omitted. An additional purpose is to assess the adequacy of existing wing-body interference theory (see, e.g., ref. 2) for use in estimating the aerodynamic characteristics of aircraft having wings of very low aspect ratio.

SYMBOLS

A body base area, $\frac{\pi}{4}d^2$

A_p plan-form area (including that of body)

A_W exposed wing area of two panels

AR aspect ratio, $\frac{(b - d)^2}{A_W}$

b wing span, body included

b_T tail span, body included

C_D drag coefficient, $\frac{\text{drag}}{q_\infty A}$

C_L lift coefficient based on body base area, $\frac{\text{lift}}{q_\infty A}$

$C_L{}'$ lift coefficient based on total plan-form area, $\frac{\text{lift}}{q_\infty A_p}$

$C_{L'_{B_1}}$ lift coefficient of body based on body plan-form area, $\frac{\text{lift}}{q_\infty A_p}$

C_l rolling-moment coefficient (see fig. 1(e)), $\frac{\text{rolling moment}}{q_\infty A_W b}$

C_m pitching-moment coefficient about station 4d ahead of body base (see fig. 1(e)), $\frac{\text{pitching moment}}{q_\infty A d}$

C_n yawing-moment coefficient about station 4d ahead of body base (see fig. 1(e)), $\frac{\text{yawing moment}}{q_\infty A d}$

C_Y side-force coefficient, $\frac{\text{side force}}{q_\infty A}$

c_r root chord at wing-body juncture

d body base diameter

f_n fineness ratio of body nose, $\dfrac{l_n}{d}$

l body length

l.e.   leading edge

l_n body nose length (see fig. 1(a))

M_∞ free-stream Mach number

q_∞ free-stream dynamic pressure

R   Reynolds number based on body length

r   local body radius

x,y,z   Cartesian coordinates as shown in figure 1(e)

$\bar{x}$ controid of plan-form area measured from tip of body nose

x_p center of pressure measured from tip of body nose

α angle of attack measured between body axis and free-stream
          direction (see fig. 1(e))

ϵ wing semiapex angle

φ angle of bank about x axis (see fig. 1(e))

APPARATUS AND TESTS

Wind Tunnels

The experimental investigation was conducted in the Ames 1- by 3-foot
supersonic wind tunnels no. 1 and no. 2. Tunnel no. 1 is a closed-circuit,
continuous-operation type and is equipped with a flexible-plate nozzle that
provides a variation of Mach number from 1.4 to 4.0. The Reynolds number
is changed by varying the total pressure within the approximate limits of
1/5 of an atmosphere to 4 atmospheres. Tunnel no. 2 is a nonreturn,
intermittent-operation type and is also equipped with a flexible-plate
nozzle that provides a variation of Mach number from about 1.4 to 3.8.
Air for this tunnel is obtained from the Ames 12-foot wind tunnel at a
pressure of about 6 atmospheres and is expanded through the nozzle to the
atmosphere. Changes in Reynolds number are obtained by varying the total
pressure.

The water content of the air in both the 1- by 3-foot wind tunnels is maintained at less than 0.0003 pound of water per pound of dry air. Consequently, the effect of humidity on the flow is negligible.

Models

The models studied are shown in figure 1. Both cruciform and monowing arrangements were tested. The basic body (B_1) had a total fineness ratio of 10, being composed of a fineness-ratio-3 tangent-ogive nose and a cylindrical afterbody. In some instances, the models were also tested with an approximate Newtonian minimum-drag nose of fineness ratio 5, resulting in a body (B_2) of total fineness ratio of 12. In figure 1(a), body B_1 is shown with triangular wings and a tail (T) which could be used for control. Five triangular wings having aspect ratios from 3/32 to 1 were used. These wings are identified in figure 1(a) by W_1, W_2, W_3, W_4, and W_5. The wing sections were flat plates with leading and trailing edges generally beveled to small radii. In some cases, the leading edges were rounded with relatively large radii. (See sketches of leading edges in fig. 1(a).) In figure 1(b), body B_1 is shown with curved leading-edge wings, W_6, W_7, and W_8. The exposed plan-form areas of these wings and wing W_3 are all equal. These wings were also constructed with beveled leading and trailing edges. Canard surfaces which were mounted on the nose of body B_1 for certain tests are shown in figure 1(c). These surfaces, which are of triangular plan form with semiapex angles of 14°, are of two sizes. With the smaller surfaces attached, the body is identified by B_1S, and with the larger surfaces attached, the body is identified by B_1L.

All models were constructed of steel and were sting supported from the rear. A photograph of a typical model (B_1W_3T) mounted in the wind tunnel is shown in figure 1(d).

Tests

Force tests.- Force data were obtained in tunnel no. 2 for the models at free-stream Mach numbers of 1.97 and 3.33. The Reynolds number, which was maintained constant for all tests, was about 9×10^6 based on the length of the basic body B_1. The angle-of-attack range was from 0° to 17° for Mach number 1.97 and from 0° to 30° for Mach number 3.33.

At various angles of attack, measurements of lift, drag, pitching moment, and rolling moment were taken. For certain model configurations side-force and yawing-moment measurements were also obtained at angles of bank of 22.5° and 45°. Base pressures from eight orifices evenly spaced around the inside of the base periphery were photographically

recorded from a multiple-tube manometer system. The repeatability of
force and pressure measurements was checked by making reruns for several
configurations.

Vapor-screen tests.- To make vortices shed from models visible, use
has been made of a technique which has been termed the "vapor-screen"
method (ref.3). With this technique, vortices which are shed from inclined
models are made visible at various longitudinal positions by the intro-
duction of water vapor into the tunnel air stream. This water vapor con-
denses in the wind-tunnel test section to produce a fine fog. A narrow
sheet of bright light, produced by high-intensity mercury-vapor lamps, is
projected through the tunnel window in a plane essentially perpendicular to
the tunnel axis. This plane of light appears as a uniformly lighted screen
of fog particles in the absence of a model. However, with a model in the
stream, the flow about the model affects the light scattered by the water
particles, and vortices shed from the model are visible as dark spots.

Vapor-screen tests were made in tunnel no. 1 for various models at
Mach number 3.33. With the models at several angles of attack, the
vortex patterns were photographed with a camera mounted inside the wind
tunnel about 8 inches downstream from the base of the models.

China-clay tests.- Another method of flow visualization used was
the "china-clay" technique (ref.4) for locating separation and vortex
traces on the models. For these tests, the models were first given a
white appearance by being sprayed with a mixture of china clay and lacquer
thinner. Then a wetting agent, eugenol, was sprayed on to give a black
appearance which changes to white as the eugenol dries. The presence of
separation and vortices is determined as black areas on the model. All
china-clay tests were made in tunnel no. 1 at Mach number 3.33. China-clay
photographs of the models tested at 15° angle of attack are presented in
this report.

REDUCTION AND ACCURACY OF DATA

All of the force and moment data have been reduced to coefficient form
and are referred to the coordinate system shown in figure 1(e). The base
drag was computed using the average base pressure and was subtracted from
the total axial-force measurement, so that the data presented are for
forces ahead of the body base.

The accuracy of the final data is affected by uncertainties in the
measurement of the forces and moments, and in the determination of the
stream static and dynamic pressures used in reducing the forces and moments
to coefficient form. These individual uncertainties led to estimated
uncertainties in the various force and moment coefficients which are listed
in the following table:

Coefficient	Uncertainty
C_L	±0.08
C_D	±.02
C_m	±.25
x_p/d	±.08
C_Y	±.08
C_n	±.25
C_l	±.002

The values of angle of attack are estimated to be accurate to within ±0.1°. The variation of the free-stream Mach number in the region of the test models was less than ±0.01 at Mach number 1.97 and less than ±0.04 at Mach number 3.33.

RESULTS AND DISCUSSION

This section of the report is divided into three parts: experimental force and moment characteristics, comparisons of theory and experiment, and results of visual flow studies. The experimental aerodynamic characteristics are presented in figures 2 through 14; comparisons of theory and experiment are presented in figures 15 and 16; and pictures of the flow over the models are shown in figures 17 and 18.

Experimental Force and Moment Characteristics

Effect of aspect ratio and wing area.- The effects of simultaneous change in aspect ratio and wing area on the lift, drag, pitching moment, and center of pressure of the missiles having triangular cruciform wings are presented in figures 2 and 3 for Mach numbers 1.97 and 3.33. For these configurations the wing root chord is constant; hence increases in wing aspect ratio result in increases in plan-form area. The reader is reminded that the coefficients are based on body dimensions, which remain fixed regardless of wing plan form. In view of this fact, it is not surprising that the lift coefficient of the missiles increases at all angles of attack with increase in wing aspect ratio. (See figs. 2(a) and 3(a).) The question arises, then, of whether or not the lift effectiveness, or lift per unit plan-form area, also increases with the addition of small wings to a body. In figure 13, lift coefficients based on total missile plan-form area including that of the body rather than on body cross-sectional area (as in figs. 2 and 3) are presented as a function of angle of attack. For clarity, the experimental data points have been omitted. The ratio of the lift coefficient of each missile to that of the body (B_1)

is also presented as a function of angle of attack for both Mach numbers 1.97 and 3.33. Even the smallest wing (aspect ratio 3/32) increases the lift effectiveness appreciably over that for the body. At Mach number 1.97 the addition of the smallest wing (W_1) to the body (B_1) results in increases in lift effectiveness of greater than 40 percent throughout the entire angle-of-attack range. From the plots in figure 13, it is clear that the effectiveness of winged compared to wingless missiles increases rapidly with decrease in angle of attack in the lower angle-of-attack range (below about 8°). The plots also illustrate the greater effectiveness of winged missiles at Mach number 1.97 than at Mach number 3.33. However, even at Mach number 3.33 and high angles of attack, the lift effectiveness is greater for the winged than the wingless missiles.

Although there is the advantage of increased lift effectiveness with increased wing aspect ratio and area, there are certain disadvantages which, of course, should be considered. There may be structural, weight, handling, and packaging disadvantages which could greatly diminish the advantage of increased lift effectiveness. In addition, there are heating and other aerodynamic problems which are aggravated by an increase in wing area. One aerodynamic disadvantage, readily apparent from the data of this report, is the increase in minimum drag accompanying the increased lift effectiveness. The zero-lift drag of the missile having the wing of aspect ratio 1 (B_1W_5) is about twice that for the missile having the smallest wing (B_1W_1) or the missile having no wing (B_1) (figs. 2(b) and 3(b)). This is due primarily to the increase in skin-friction drag resulting from greater surface area for the missile with the higher aspect ratio wing.

The effect of changes in aspect ratio and area on the pitching moment and center of pressure is shown in figures 2(c), 2(d), 3(c), and 3(d). The center of pressure for the body (B_1) starts near the centroid of the nose at zero angle of attack and then moves rearward toward the centroid of the complete body ($x = 5.47d$) as the angle of attack is increased. Adding even the smallest wing results in a rearward shift of the center of pressure at all angles of attack. It is also apparent that the addition of wings of low aspect ratio results in smaller center-of-pressure shifts than those of the body alone. Of particular importance is the finding that the use of a wing of relatively low aspect ratio (of the order of only 3/8) results in practically no movement in center of pressure with angle of attack. From a comparison of figures 2(d) and 3(d), it can be seen that the center of pressure for the missile (B_1W_3) having the wing of aspect ratio 3/8 also moves very little with Mach number. For this missile, the total center-of-pressure travel with the changes made in Mach number and angle of attack was less than about 0.3d. The small center-of-pressure shifts associated with these configurations simplify the problems of stability and control.

Effect of variations in wing plan-form shape.- The effect of some variations in wing plan-form shape on the aerodynamic characteristics of missiles having low-aspect-ratio wings also has been studied. Tests have

been made of configurations $(B_1W_6, B_1W_7,$ and $B_1W_8)$ whose wings are equal
in area to the triangular wing of aspect ratio 3/8, although the leading
edges are curved in plan form rather than straight. (See fig. 1(b).)
Aerodynamic characteristics for these missiles are compared in figures 4
and 5 with those previously presented for the missile (B_1W_3) employing
the triangular wing of aspect ratio 3/8.

It is interesting to note that for Mach number 1.97 there are impor-
tant differences in lift between the various configurations (fig. 4(a)).
These differences are in qualitative agreement with slender-body theory
which predicts an increase in lift-curve slope with increase in span. The
greatest lift at all angles of attack was developed by the missile having
the concave leading-edge wing and the greatest span (B_1W_7). The least lift
was developed by the missile with the wing extending all the way to the bow
of the nose and having the least span (B_1W_8). For a given value of lift
coefficient, the missile with the wing extending to the bow of the body
(B_1W_8) also had the most drag, whereas the missile with the concave
leading-edge wing (B_1W_7) had the least (fig. 4(b)). The lift and drag
advantages of missile configuration B_1W_7 over the other configurations,
although of importance at Mach number 1.97, almost disappear at Mach
number 3.33. (Compare figs. 4(a) and 4(b) with 5(a) and 5(b).)

Possibly of greater importance than the lift and drag differences
between these missiles are the pitching-moment and center-of-pressure dif-
ferences. (See figs. 4(c), 4(d), 5(c), and 5(d).) The missile with the
wing extended to the tip of the nose (B_1W_8) has the greatest center-of-
pressure travel with angle of attack. For all of these configurations,
as the centroid of plan-form area is shifted rearward, the center-of-
pressure position is also shifted rearward, the variation being almost
linear at both Mach numbers. This is, perhaps, best illustrated in figure
14, where center-of-pressure positions at various angles of attack are
plotted as a function of centroid of plan-form area. The center-of-
pressure travel with angle of attack generally decreases as the missile
centroid is moved aft. The travel is least for the missile with the con-
cave leading-edge wing (B_1W_7). However, even though the center-of-pressure
movement with angle of attack is least for missile B_1W_7 at each Mach num-
ber, it is not the smallest with change in Mach number. With both change
in Mach number and angle of attack considered, the center-of-pressure
travel for the missile with the straight leading-edge wing (B_1W_3) is the
smallest.

Effects of change of body nose and wing bluntness.- The effects of
changes in body nose shape and wing leading-edge bluntness on the aerody-
namic characteristics of missiles are important to the designer considering
performance. Since a large portion of the drag of missiles employing low-
aspect-ratio wings can be attributed to the body nose, the choice of nose
shape and fineness ratio is important. It is well known that nose pressure
drag can be reduced by increasing nose fineness ratio or, for a fixed fine-
ness ratio, by using a shape contoured to give theoretical mimimun drag.

(See, e.g., ref. 5.) The effect of changing the nose of two missiles, one having a wing of aspect ratio 1 and the other an aspect ratio of 3/8, is shown in figures 6 and 7. The data in figure 6 are for a Mach number of 1.97, and the data in figure 7 are for a Mach number of 3.33. Changing the nose from a tangent ogive of fineness ratio 3 to a Newtonian minimum-drag shape of fineness ratio 5 results in an appreciable decrease in minimum drag with little change in center-of-pressure position relative to the body base.

The effect of changing from a wing section with a relatively sharp leading edge to a section having a blunt (rounded) leading edge was negligible, even for the missile having the wing of least sweep (W_5). This is seen in figure 6, where the results for the monowing configuration B_1W_{5M} with the sharp leading-edge wing are compared with those for the monowing configuration B_1W_{5M} with the rounded leading-edge wing. These results, together with unpublished data at $M = 3$, indicate that large drag penalties will not be incurred by blunting the leading edges of these highly swept wings to alleviate aerodynamic heating.

Effects of canard and tail surfaces.- The effects of undeflected canard and tail surfaces on the aerodynamic characteristics of the missile (B_1W_3) with the wing of aspect ratio 3/8, are presented in figures 8 and 9. As expected, the lift and drag coefficients for this missile are not significantly affected by the addition of small canard or tail-control surfaces. The already small center-of-pressure shift associated with configuration B_1W_3 is even further reduced by the addition of the small canard surfaces. This result is in agreement with the finding of the Douglas Aircraft Company (ref. 6) as concerns the use of small fixed surfaces forward of the wing to reduce center-of-pressure travel. The effectiveness of the tail surfaces in controlling the missile is discussed in reference 1.

Effect of angle of bank.- The effect of angle of bank on the aerodynamic characteristics of various cruciform and monowing configurations at Mach number 3.33 is illustrated in figures 10, 11, and 12. Data are presented for bank angles of 22.5° for cruciform and 45° for monowing models, since maximum rolling moments occur close to these angles. For all configurations having cruciform wings there are only small changes in lift, pitching moment, and center of pressure with changes in bank angle. Slender-body theory predicts no variation of these quantities with bank angle. As expected, the side forces and yawing moments due to roll are greater for the missile having the wing of aspect ratio 1 (B_1W_5) than for the missiles having the smaller wing of aspect ratio 3/8 (B_1W_3 and B_2W_3).

Comparisons are made in figure 11 between the cruciform configuration B_1W_3 and the monowing configuration B_1W_{3M}, both of which have wings of aspect ratio 3/8. Since at zero bank the only difference between the characteristics for the cruciform and monowing arrangements is in drag, and the $\varphi = 0$ drag results are not available for B_1W_{3M}, none of the zero-bank results for B_1W_{3M} are presented in figure 11. For the

missiles in roll, small reductions in lift result with the use of the
cruciform arrangement, whereas large reductions result with the monowing.
The effect of roll on the longitudinal center-of-pressure travel is neg-
ligible for the cruciform but fairly large for the monowing arrangement
(fig. 11(d)). (The curve for $\varphi = 0^\circ$ applies to both the monowing and
cruciform configurations.) The forward center-of-pressure travel with
bank of the monowing configuration must result from loss of wing lift
since the lift over the nose is unaffected by banking the model. Because
of the increased projected surface area in the pitch plane, the cruciform
missile develops greater side forces than the monowing (fig. 11(e)). The
zero slope at $\alpha = 0$ of the side-force curve for the monowing is in accord
with slender-body theory.

In figure 12 the effect of various wing and nose arrangements on roll-
ing moments is illustrated. Rolling-moment coefficients, based on exposed
wing area of two panels and total span, are plotted as a function of angle
of attack. As previously mentioned, the data were taken for roll angles
of 22.5° for the cruciform and 45° for the monowing models, since maximum
rolling moments occur close to these roll angles. The rolling moments
are considerably larger and opposite in sign for the monowing as compared
to the cruciform arrangement with the same body. The dihedral effect is
positive for the monowing and negative for the cruciform arrangement.
For the cruciform arrangement, the model with the longer nose (B_2W_3) had
larger rolling moments than the model with the shorter nose (B_1W_3). This
indicates that long noses or forebodies extending in front of the wings
are undesirable if induced rolling moments are to be minimized.

Comparisons of Theoretical and Experimental
Force and Moment Characteristics

In this section of the report, theoretical methods of estimating the
aerodynamic characteristics of missile configurations employing wings of
very low aspect ratio are assessed by comparing computed results with
experimental data. All comparisons are presented in figures 15 and 16 and
are discussed in the following paragraphs.

Body alone.- For the body alone (B_1), the lift and drag were computed
by the crossflow theory of Allen (ref. 3). In this theory the lift by
slender-body potential theory is added to an additional crossflow lift
attributed to the separation effects of viscosity. Basically it is assumed
that the flow over a body can be resolved into two components, namely, a
flow perpendicular to the body axis and a flow parallel to it. The viscous
crossflow is considered to be independent of the axial flow and to be that
of the steady flow past a circular cylinder. Although this procedure has
been shown experimentally to be only approximate (ref. 7), the method has
provided a considerable improvement at high angles of attack over the use

of potential theory. The lift for body B_1, computed by Allen's method, is in quite good agreement with experiment. (See figs. 15(a) and 16(a).)

In computing the drag characteristics, the zero-lift drag was taken as the sum of the skin-friction and pressure drag. Either completely laminar (ref. 8) or completely turbulent (ref. 9) flat-plate skin-friction drag has been assumed. The pressure drag was determined from reference 10, having been originally computed by the method of characteristics. For the body at angle of attack, the drag rise determined by Allen's method has been added to the zero-lift foredrag for comparison with experiment. The agreement between theory and experiment is good.

For simplicity, comparisons of theory with experiment for the body alone are omitted from the pitching-moment and center-of-pressure plots of figures 15 and 16. It was found that the center-of-pressure positions computed by Allen's method are between 1/2 and 1 body diameter forward of the experimental positions. A more detailed discussion of the calculation of body characteristics by the use of various methods is presented in reference 7.

Body with cruciform wings of triangular plan form.- The interference theory of Nielsen (see e.g., ref. 2) has been used in calculating the aerodynamic characteristics for the missiles having triangular wings of low aspect ratio. This theory applies for slender and nonslender configurations and supplies interference factors to be applied to wing-alone and body-alone data. In applying Nielsen's method, the most reliable values of body-alone and wing-alone lift and pitching moment should be used. The adequacy of this theory for use in computing force and moment characteristics for many configurations employing wings of higher aspect ratio than those reported herein has been demonstrated previously.

The comparisons of theory with experiment are shown in figures 15 and 16. For all of the computed curves, experimental body-alone data have been used in conjunction with wing-alone results from either linear theory, Brown and Michael vortex theory (ref. 11), or from available experiment. The missile lift coefficients computed using the theory of Brown and Michael for the wings are overestimated at all angles of attack. This is expected since the theory of Brown and Michael overestimates wing-alone lift. Generally, the characteristics computed by using both experimental body-alone and wing-alone results are in the best agreement with the experimental results. (These comparisons, however, are limited because experimental wing-alone data were available only for the wings of aspect ratio 3/8 and 1.)

The drag characteristics at zero angle of attack were estimated by adding the skin-friction drag for the entire surface to the body pressure drag. The pressure drag for these highly swept thin wings was small enough in comparison with other components of drag to be neglected.

The comparisons shown in figures 15 and 16 indicate the need for further investigation into the prediction of aerodynamic characteristics for wings of low aspect ratio and missiles employing wings of low aspect ratio. The development of an additional wing-body interference method appears to be desirable. Because of the complicated nature of the flow, as discussed in the following section, an improved method probably will have to account for the effects of body and wing vortices and their interactions.

Visual Observations of Flow Over Models

To supplement the force and moment results with studies that aid in giving a physical representation of the flow, vapor-screen and china-clay tests were made for the body alone (B_1) and in combination with triangular wings. Vapor-screen and china-clay photographs of the models tested at Mach number 3.3 are presented in figures 17 and 18. As mentioned previously, the vapor-screen pictures were taken with a camera mounted inside the tunnel just downstream of the models. The china-clay pictures of the models were taken immediately following tunnel shutdown.

Vapor-screen results.- In the vapor-screen photographs of figure 17(a), vortices shed from the bodies and wings of the models at $\alpha = 15^\circ$ are shown at various length positions (x) along the body axis. The growth in size of the regions of vorticity with distance downstream can be clearly seen. For the body alone, a symmetrical pair of vortices develop from the nose. These vortices appear to increase in size and move away from the body with travel downstream. (For a more detailed study of the vortex paths and flow field about a body of revolution, the reader is referred to ref. 12.) For the body with the triangular cruciform wings at $\varphi = 0^\circ$, the body vortices are still clearly defined at $x = 5d$. Rearward of this position, however, the body vortices tend to coalesce with the wing vortices, so that at the tail position $(x = 9.63d)$ only one large region of vorticity is observed above each horizontal wing panel. It is interesting to note that these regions of vorticity flatten out and decrease in height above the horizontal wings as the aspect ratio increases. For example, compare the vortex regions at the tail of model B_1W_1 (aspect ratio of 3/32) with those at the tail of model B_1W_5 (aspect ratio of 1).

In the vapor-screen photographs of figure 17(b), the effect of angle of attack on the vortex regions is indicated. It is seen that the sizes of the vortex regions above the wings greatly increase with increase in α from 10° to 19°. It is interesting to note that, in addition to the large regions of vorticity on top of the wings, there are indications of small vortices located under the wings and near the body. (See, e.g., B_1W_5 at $\alpha = 19^\circ$). These smaller vortices probably originate at the forward

wing-body juncture. Evidence of their existence and origin is also visible from the china-clay results. (See the bottom views of B_1W_3 and B_1W_5 in figure 18.)

In figures 17(c) and 17(d) the effect of angle of bank on the vortex patterns for model B_1W_{5M} can be observed for α's of 15° and 19°. As this model (having a monowing of aspect ratio 1) is banked from $\varphi = 0^O$ to $\varphi = -22.5^O$, the left wing vortex region moves away from the left body vortex. This body vortex remains in about the same position as it would for the body alone. If an air-breathing engine or a vertical fin were to be mounted directly above the body in what would normally appear to be a vortex-free region at $\varphi = 0^O$, it would move into the path of this body vortex if the missile were banked to $\varphi = -22.5^O$.

In almost all of the photographs of figure 17 there appear to be wake shock waves similar to those indicated in reference 12. These shock waves which come from the vortex regions apparently are formed when the cross-flow Mach number ($M_\infty \sin \alpha$) exceeds about 0.5.

China-clay results.- Separation and vortex regions for models B_1, B_1W_3, and B_1W_5 determined by the china-clay technique are shown in the photographs of figure 18. Top, side, and bottom views for the models at an angle of attack of 15° are presented. The bottom of body B_1 was all white, and no picture of this view was taken.

For the body alone the regions of flow separation are clearly defined. The flow first separates on the top of the body at the nose vertex, and then the separation region moves around the body toward the windward side with travel downstream. Evidence of the two symmetrical body vortices observed in the vapor screen can be seen on the top of the body. (Note the two almost parallel black lines which appear to originate at about the nose-cylinder juncture.)

With the triangular cruciform wings attached to the body, the pattern over the afterbody is considerably changed. It appears that the two body vortices become integrated with the vorticity from the wings as previously indicated by the vapor-screen results. The markings under the wings, when considered together with the vapor-screen results, indicate separation and formation of additional vortices. It is interesting to note that evidence of upwash also is observed on the afterbodies rearward of the trailing edges of the wings.

CONCLUSIONS

Aerodynamic characteristics of configurations employing wings of very low aspect ratio have been measured for Mach numbers of 1.97 and 3.33 at a Reynolds number of 9×10^6. An analysis of the results has led to the following conclusions:

1. Even for missiles using very small wings, the lift advantage of winged compared to wingless missiles is appreciable.

2. In general, shifts in center of pressure for the winged missiles with changes in angle of attack, angle of bank, and Mach number are small, so that the problems of stability and control are simplified.

3. Large drag penalties will not be incurred by blunting the leading edges of the highly swept wings to alleviate aerodynamic heating.

4. For the configurations having wing plan forms of equal area, changes in plan-form shape and span have important effect on the lift and drag at Mach number 1.97 but little effect at Mach number 3.33. At both Mach numbers, the center-of-pressure positions are significantly influenced by changes in plan-form shape, these positions varying almost linearly with changes in centroid of missile plan-form area.

5. Increases in lift and decreases in drag result from increasing nose fineness ratio (forebody length). However, these advantages are somewhat offset by greater induced rolling moments caused by the use of the longer noses and forebodies.

6. For the cruciform arrangement, small loss of lift and little change in center of pressure results from changing the bank angle from zero (as predicted by slender-body theory), whereas for the monowing arrangement there is large loss of lift and appreciable center-of-pressure movement. Maximum rolling moments are also considerably smaller for the cruciform than for the monowing arrangement.

7. The aerodynamic characteristics can be estimated only fairly well by present wing-body interference theory, and then only if experimental body-alone and wing-alone values of lift and pitching moment are used.
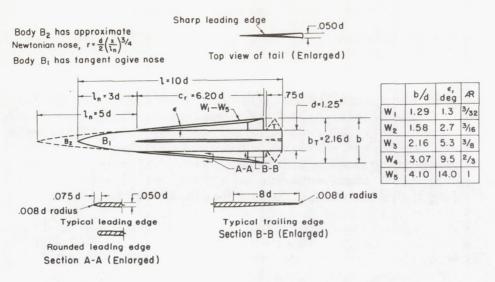
Ames Aeronautical Laboratory
    National Advisory Committee for Aeronautics
        Moffett Field, Calif., July 16, 1956

REFERENCES
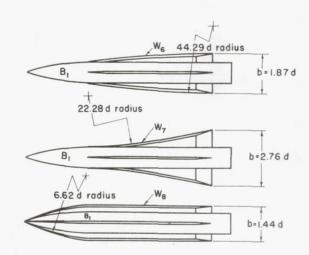
1. Katzen, Elliott D., and Jorgensen, Leland H.: Aerodynamics of Missiles Employing Wings of Very Low Aspect Ratio. NACA RM A55L13b, 1956.

2. Nielsen, Jack N., Kaattari, George E., and Anastasio, Robert F.: A Method for Calculating the Lift and Center of Pressure of Wing-Body-Tail Combinations at Subsonic, Transonic, and Supersonic Speeds. NACA RM A53G08, 1953.

3. Allen, H. Julian, and Perkins, Edward W.: A Study of Effects of
    Viscosity on Flow Over Slender Inclined Bodies of Revolution.
    NACA Rep. 1048, 1951.
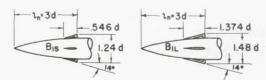
4. Gazley, Carl, Jr.: The Use of the China-Clay Lacquer Technique
    for Detecting Boundary-Layer Transition. Rep. 49A0536, General
    Electric Co., Schenectady, N.Y., Mar. 1950.

5. Jorgensen, Leland H.: Correlation by the Hypersonic Similarity
    Rule of Pressure Distributions and Wave Drags for Mimimum-Drag
    Nose Shapes at Zero Angle of Attack. NACA RM A53F12, 1953.

6. Buquoi, T. W.: Presentation of Force and Moment Data from a
    Wind Tunnel Test of an 0.0333 Scale Wing Planform Development
    Model for the 1810 Missile at Mach Numbers 1.61, 1.97, 2.54,
    and 2.80 (Phases II and III). Rep. SM-18420, Douglas Aircraft
    Co., Inc., Santa Monica, Aug. 23, 1954.

7. Perkins, Edward W., and Jorgensen, Leland H.: Comparison of Experi-
    mental and Theoretical Normal-Force Distributions (Including
    Reynolds Number Effects) On an Ogive-Cylinder Body at Mach
    Number 1.98. NACA TN 3716, 1956.

8. Blasius, H.: Grenezschichten in Flüssigkeiten mit Kleiner
    Reibung. Zeitschrift für Mathematik und Physik, vol. 56, no. 1.
    1908, pp. 1-37.

9. Rubesin, Morris W., Maydew, Randall C., and Varga, Steven A.:
    An Analytical and Experimental Investigation of the Skin
    Friction of the Turbulent Boundary Layer on a Flat Plate
    at Supersonic Speeds. NACA TN 2305, 1951.

10. Rossow, Vernon J.: Applicability of the Hypersonic Similarity
    Rule to Pressure Distributions Which Include the Effects of
    Rotation for Bodies of Revolution at Zero Angle of Attack.
    NACA TN 2399, 1951.

11. Brown, Clinton E., and Michael, William H., Jr.: On Slender
    Delta Wings with Leading-Edge Separation. NACA TN 3430, 1955.

12. Jorgensen, Leland H., and Perkins, Edward W.: Investigation of
    Some Wake Vortex Characteristics of an Inclined Ogive-Cylinder
    Body at Mach Number 1.98. NACA RM A55E31, 1955.

Body B_2 has approximate
Newtonian nose, $r = \frac{d}{2}\left(\frac{x}{l_n}\right)^{3/4}$

Body B_1 has tangent ogive nose

Sharp leading edge

$\lceil$ .050 d

Top view of tail (Enlarged)

$l = 10\,d$

$l_n = 3\,d$

$l_n = 5\,d$

$c_r = 6.20\,d$

$W_1 - W_5$

.75 d

$d = 1.25''$

ϵ

$b_T = 2.16\,d$ b

A-A   B-B

	b/d	ϵ, deg	$\mathcal{R}$
W_1	1.29	1.3	3/32
W_2	1.58	2.7	3/16
W_3	2.16	5.3	3/8
W_4	3.07	9.5	2/3
W_5	4.10	14.0	1

.075 d

.050 d

.008 d radius

Typical leading edge

Rounded leading edge

Section A-A (Enlarged)

.8 d

.008 d radius

Typical trailing edge

Section B-B (Enlarged)

(a) Straight leading-edge wings with bodies and inline tail.

W_6 44.29 d radius

B_1

b = 1.87 d

22.28 d radius

W_7

B_1

b = 2.76 d

6.62 d radius W_8

B_1

b = 1.44 d
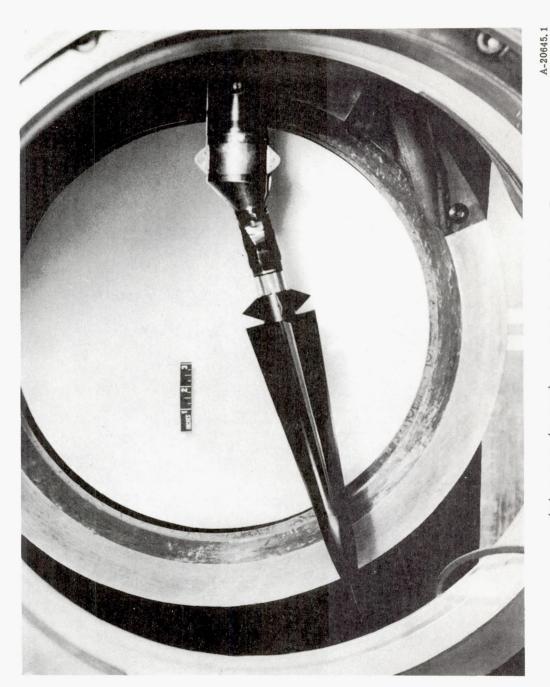
(b) Curved leading-edge wings with body B_1, (Plan-form areas of wings W_3, W_6, W_7, and W_8 are equal.)

$l_n = 3\,d$

.546 d

B_{1S} 1.24 d

14°

$l_n = 3\,d$

1.374 d

B_{1L} 1.48 d

14°
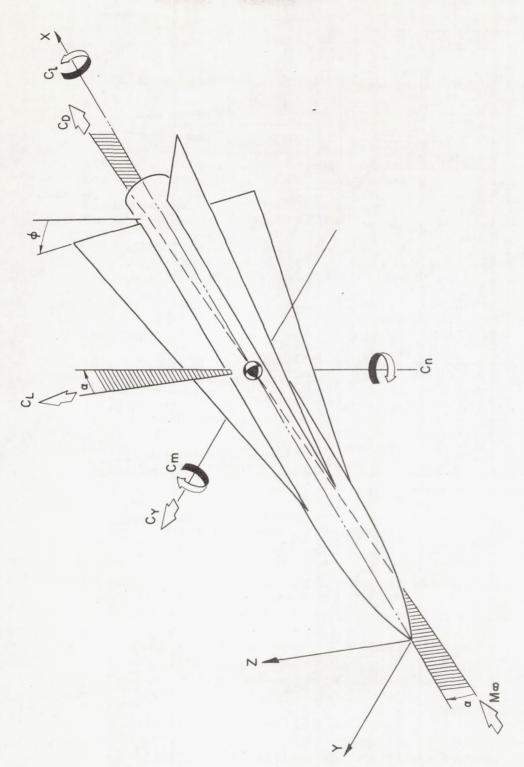
(c) Canard surfaces on nose of body B_1

Figure 1.- Missile configurations and coordinate system.

A-20645.1

(d) Model (B_1W_3T) mounted in wind tunnel.

Figure 1.-Continued.

(e) Coordinate system and sign convention.

Figure 1.- Concluded.

(a) Lift.

(b) Drag.
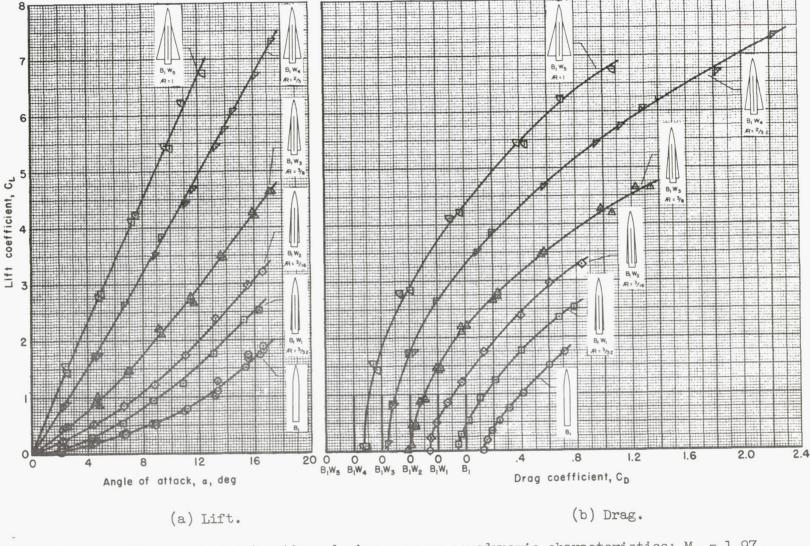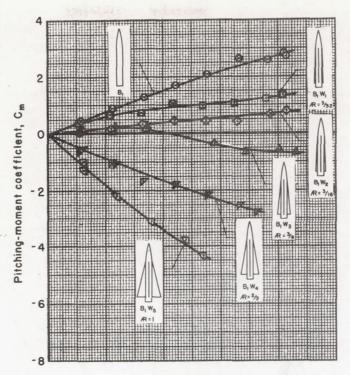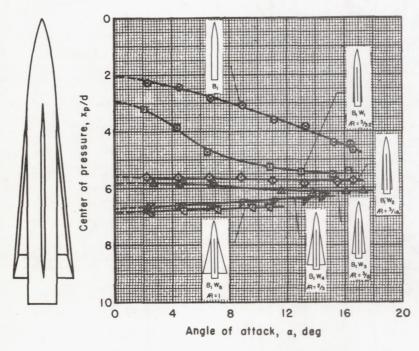
Figure 2.- Effect of aspect ratio and wing area on aerodynamic characteristics; $M_\infty = 1.97$.

(c) Pitching moment.

(d) Center of pressure.

Figure 2.- Concluded.

(a) Lift.
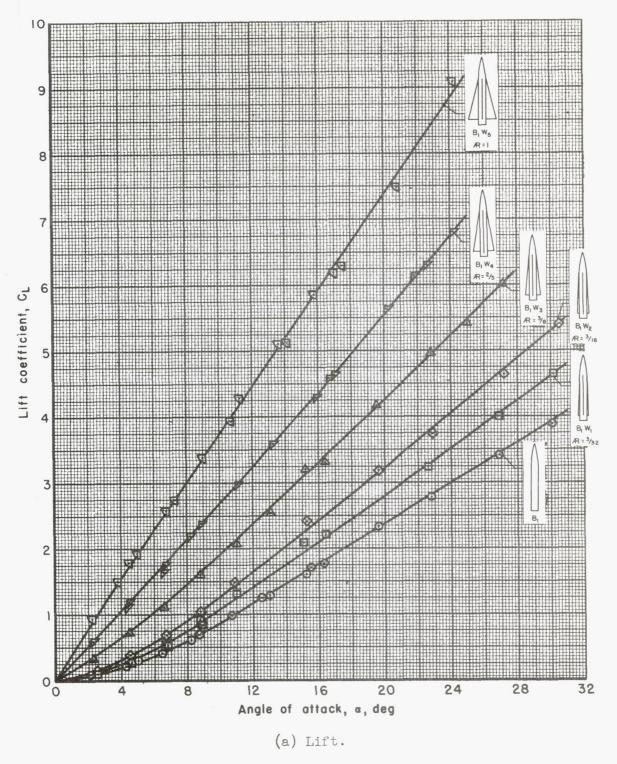
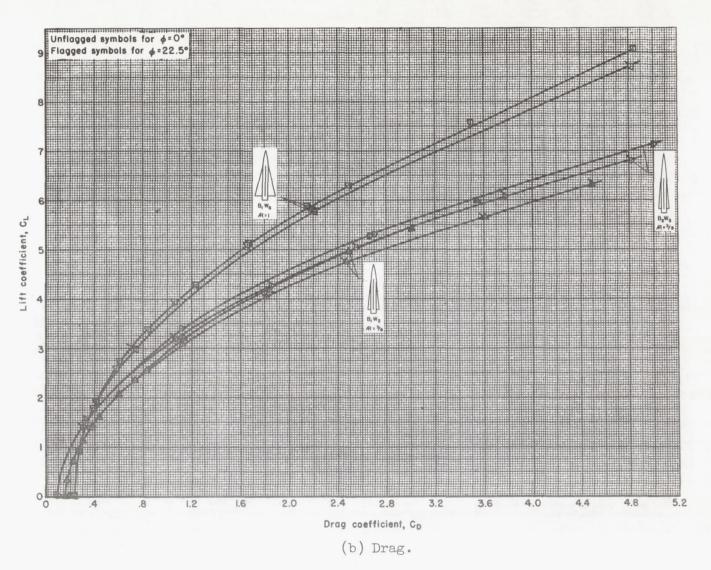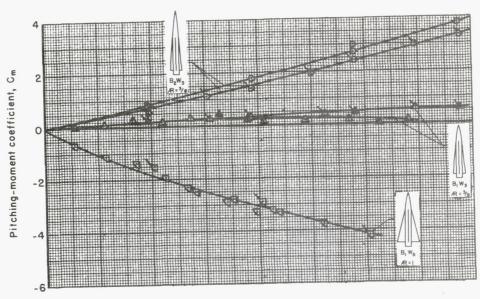Figure 3.- Effect of aspect ratio and wing area on aerodynamic charac-
teristics; M_∞ = 3.33.

(b) Drag.
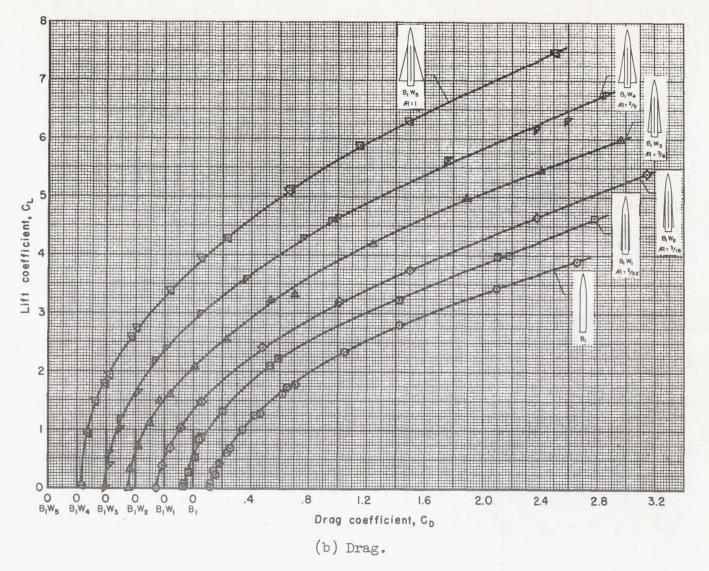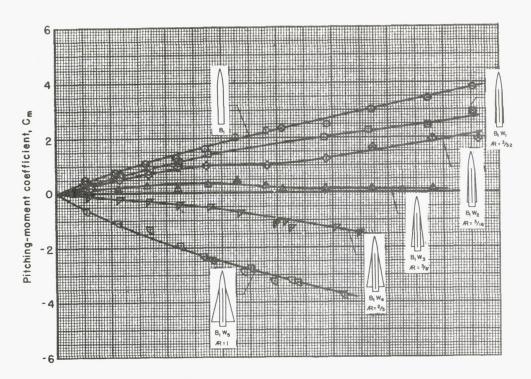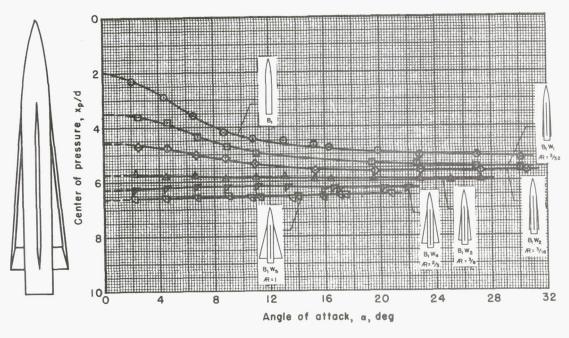
Figure 3.- Continued.

(c) Pitching moment.

(d) Center of pressure.

Figure 3.- Concluded.

(a) Lift.

(b) Drag.
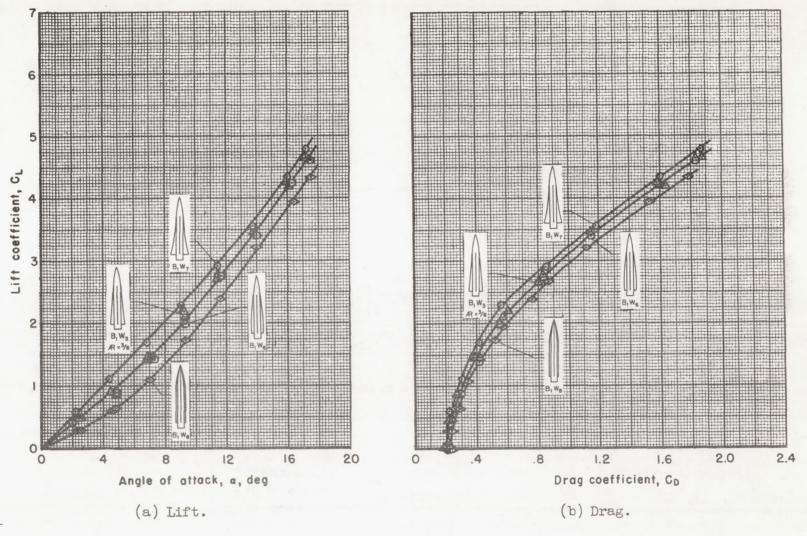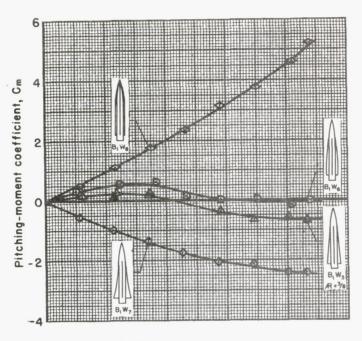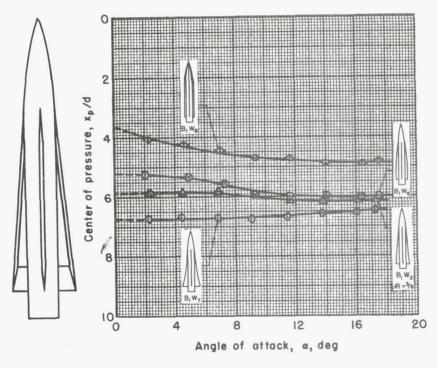
Figure 4.- Effect of variations in wing plan-form shape on aerodynamic characteristics of missiles having equal plan-form areas; $M_\infty = 1.97$.

(c) Pitching moment.

(d) Center of pressure.

Figure 4.- Concluded.

(a) Lift.
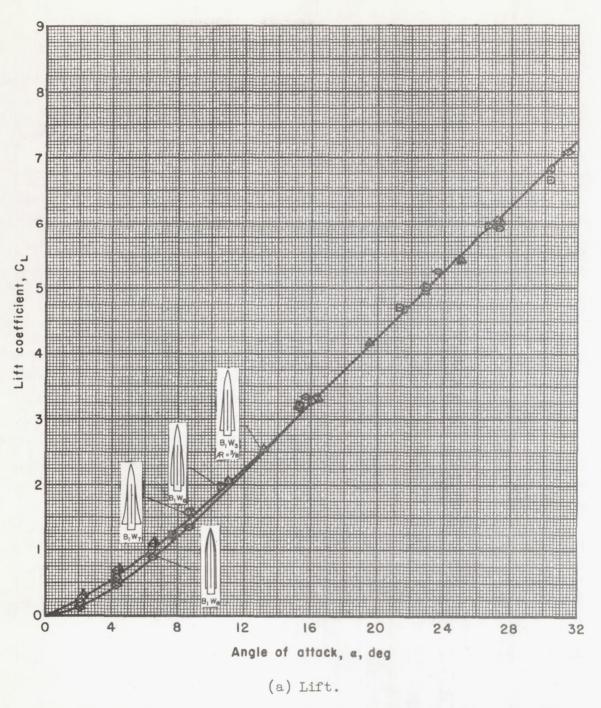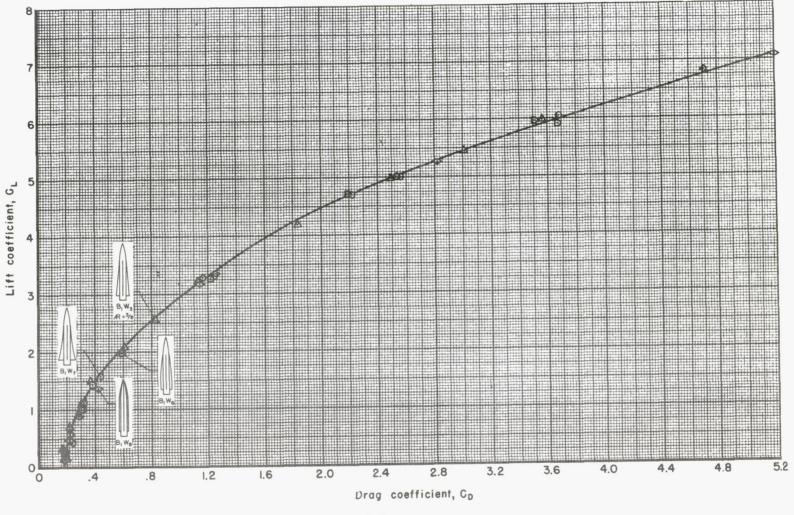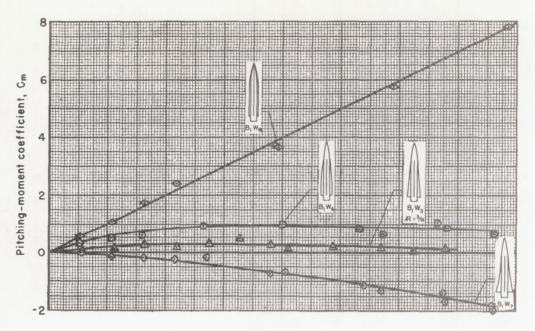
Figure 5.- Effect of variations in wing plan-form shape on aerodynamic
characteristics of missiles having equal plan-form areas; $M_\infty = 3.33$.
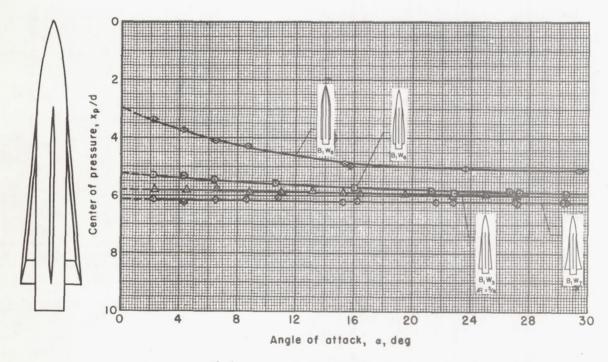
(b) Drag.

Figure 5.- Continued

(c) Pitching moment.

(d) Center of pressure.

Figure 5.- Concluded.

(a) Lift.

(b) Drag.
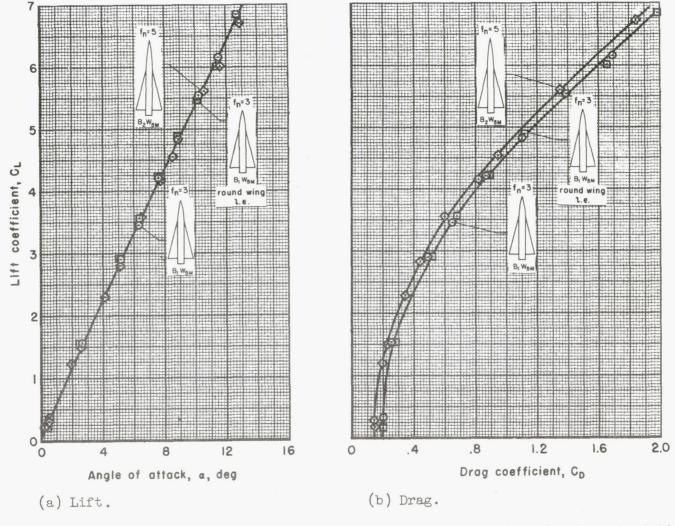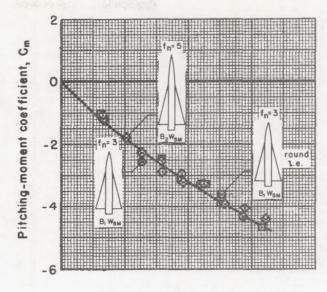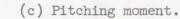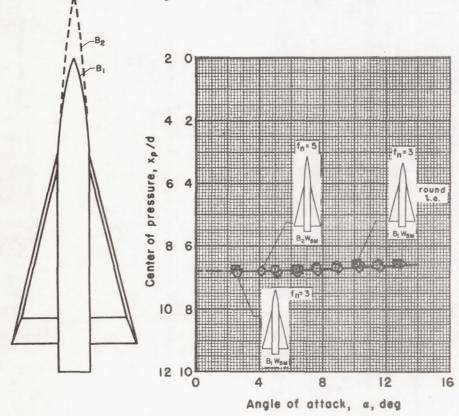
Figure 6.- Effects of change of body nose and wing bluntness on aerodynamic characteristics of a missile employing a monowing of aspect ratio 1; $M_\infty = 1.97$.

(c) Pitching moment.

Angle of attack, α, deg

(d) Center of pressure.

Figure 6.- Concluded.

(a) Lift.
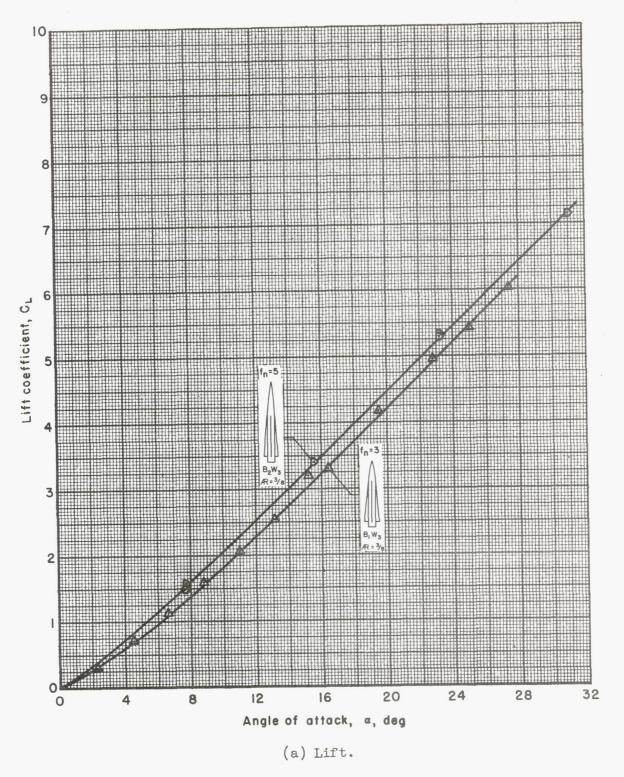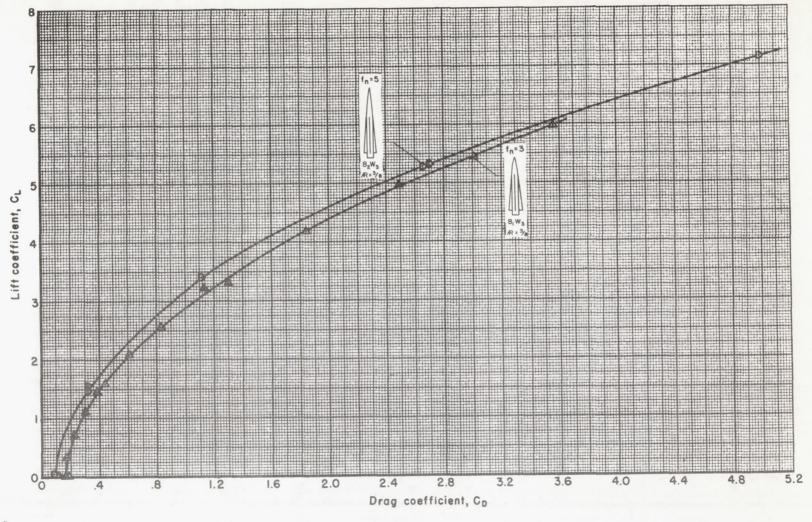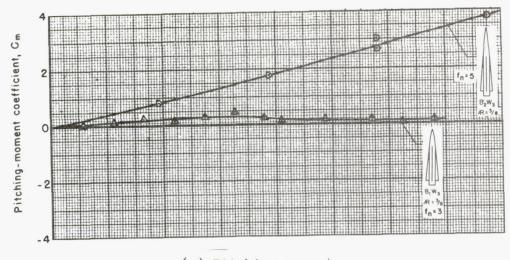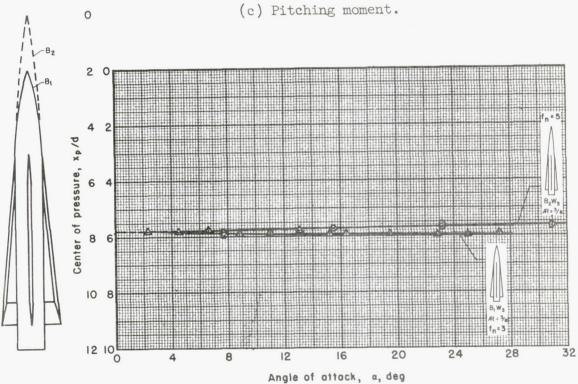
Figure 7.- Effect of change of body nose on aerodynamic characteristics
of a missile having cruciform wings of aspect ratio 3/8; $M_\infty = 3.33$.

(b) Drag.

Figure 7.- Continued.

(c) Pitching moment.

(d) Center of pressure.

Figure 7.- Concluded.

(a) Lift.

(b) Drag.
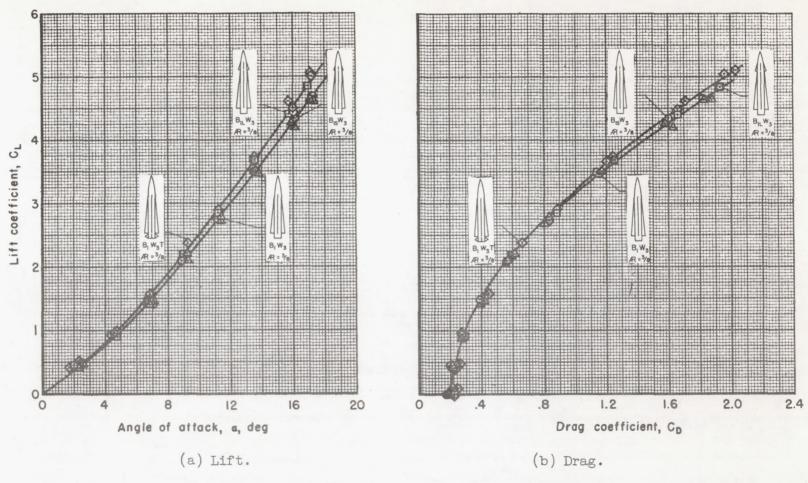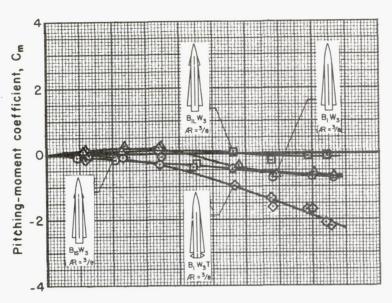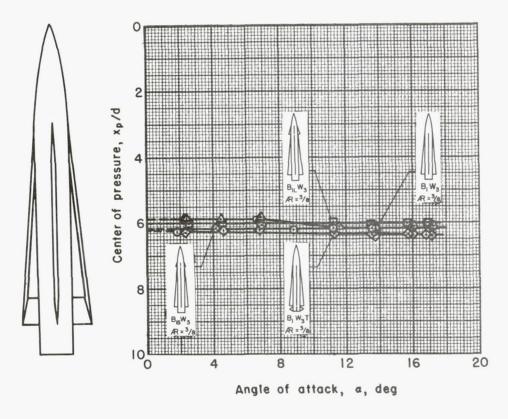
Figure 8.- Effects of canard and tail surfaces on aerodynamic characteristics of a missile employing a wing of aspect ratio 3/8; $M_\infty = 1.97$.

(c) Pitching moment.

(d) Center of pressure.

Figure 8.- Concluded.

(a) Lift.
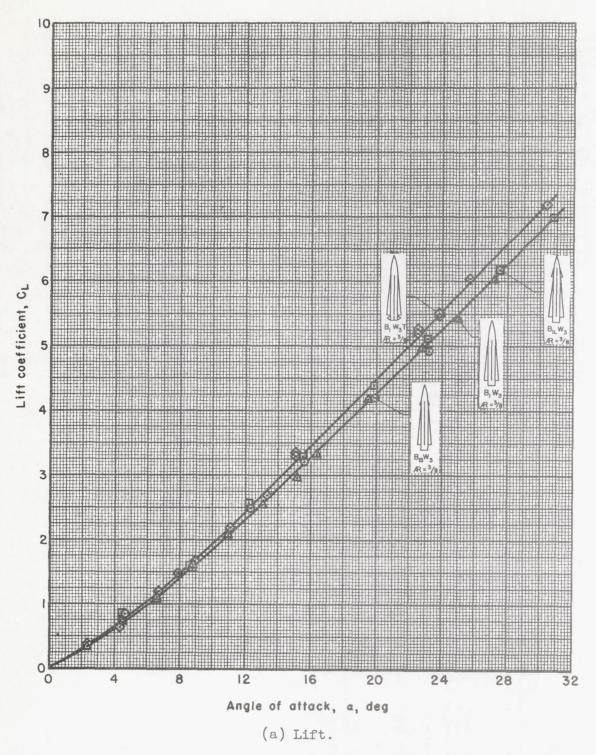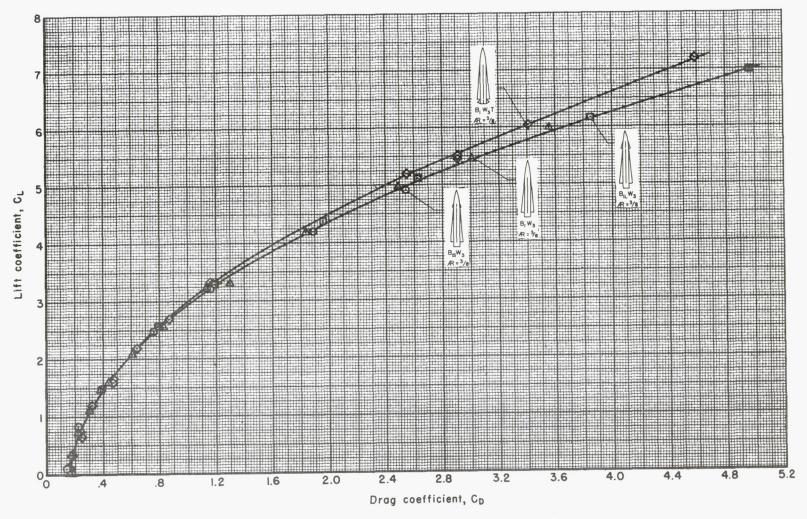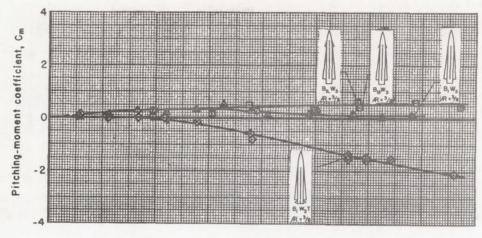
Figure 9.- Effects of canard and tail surfaces on aerodynamic character-
istics of a missile employing a wing of aspect ratio 3/8; $M_\infty = 3.33$.
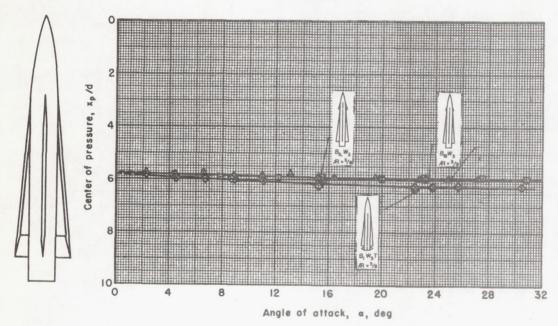
(b) Drag.

Figure 9.- Continued.

(c) Pitching moment.
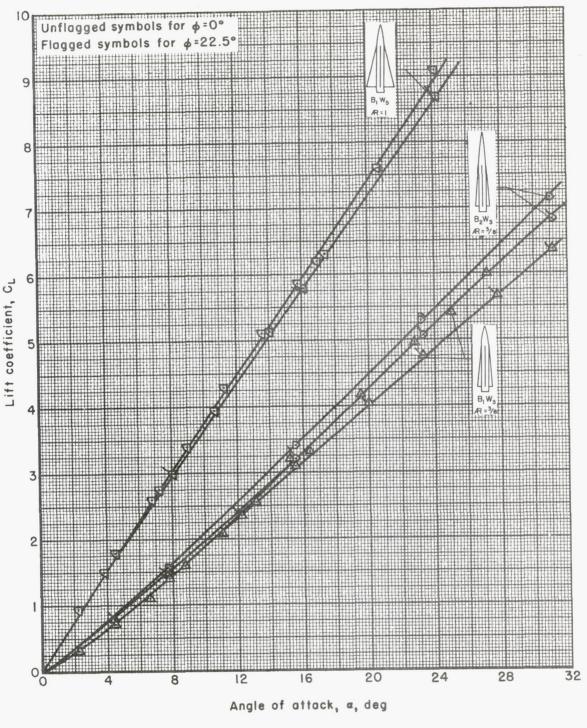

(d) Center of pressure.

Figure 9.- Concluded.

(a) Lift.

Figure 10.- Effect of angle of bank on aerodynamic characteristics of missiles having cruciform wings; $M_\infty = 3.33$.

(b) Drag.

Figure 10.- Continued.

Unflagged symbols for φ=0°
Flagged symbols for φ=22.5°

(c) Pitching moment.
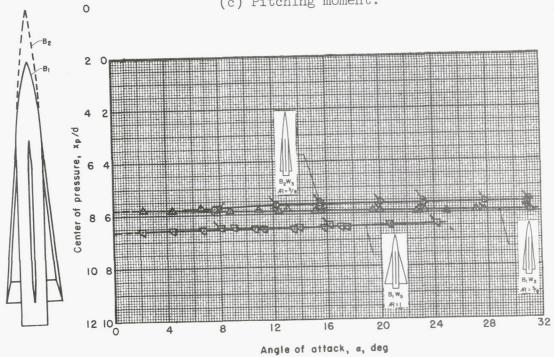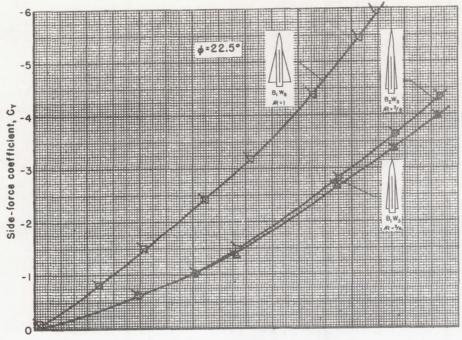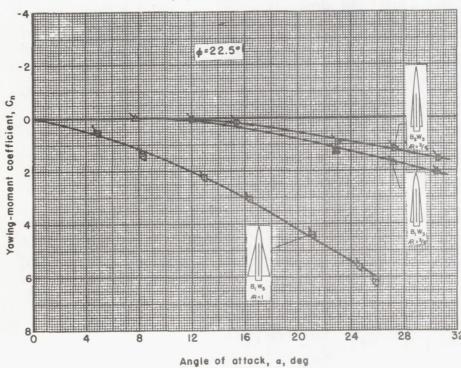
(d) Center of pressure.

Figure 10.- Continued.

(e) Side force.

Angle of attack, a, deg

(f) Yawing moment.

Figure 10.- Concluded.

(a) Lift.
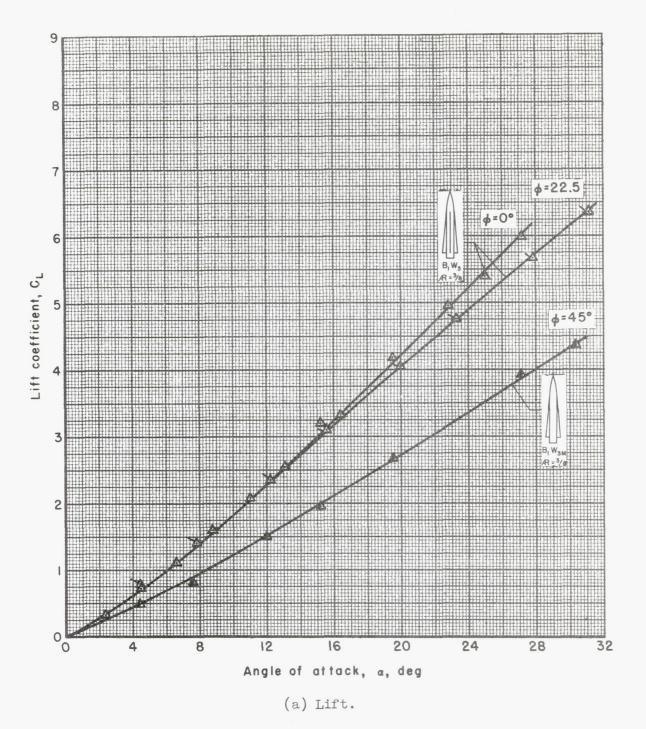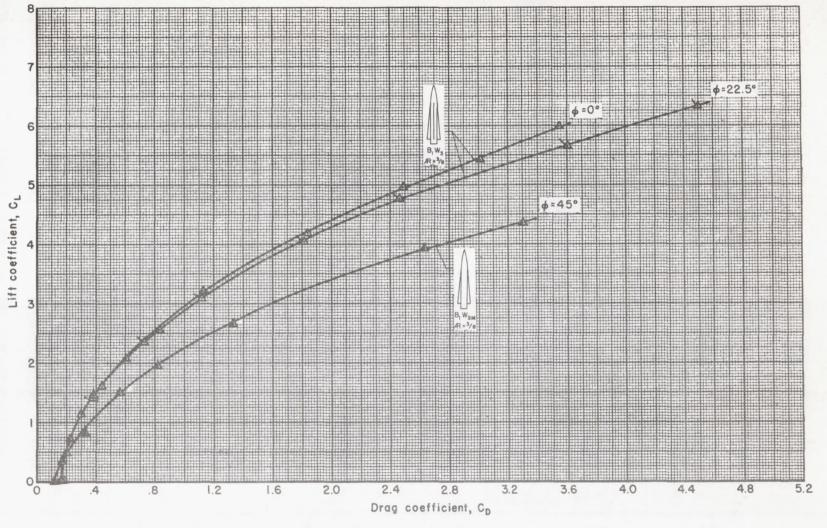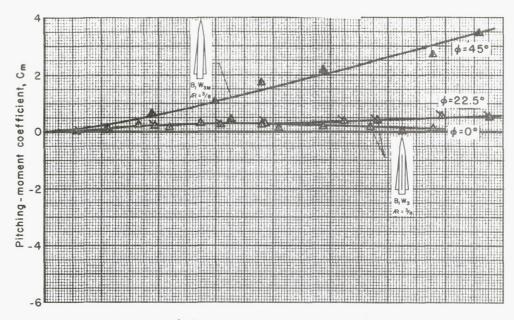
Figure 11.- Effect of angle of bank on aerodynamic characteristics of
    missiles employing cruciform and monowing (aspect ratio 3/8)
    arrangements; $M_\infty = 3.33$.
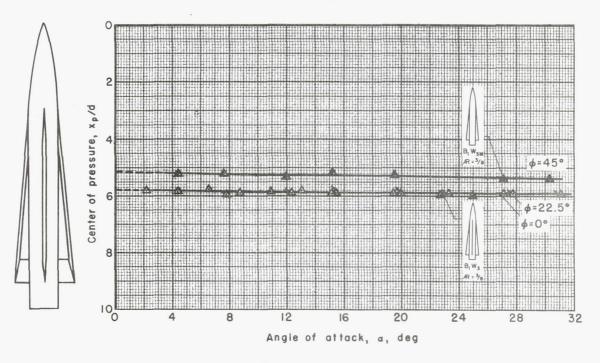
(b) Drag.

Figure 11.- Continued.

(c) Pitching moment.
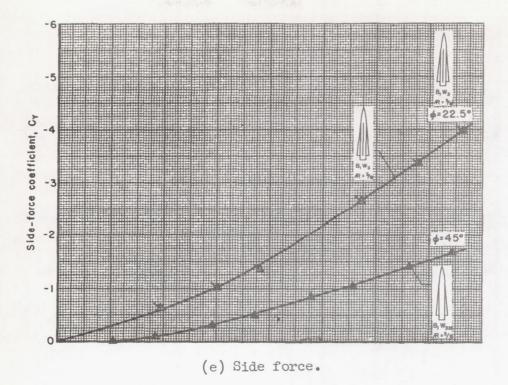
(d) Center of pressure.

Figure 11.- Continued.

(e) Side force.

(f) Yawing moment.
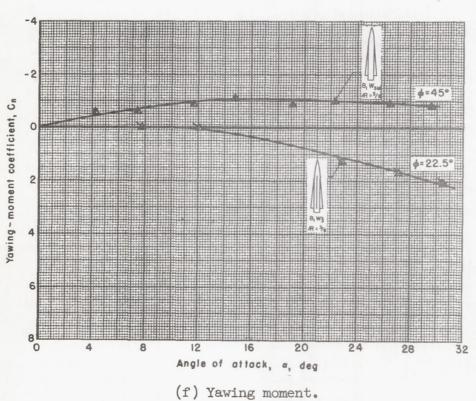
Figure 11.- Concluded.
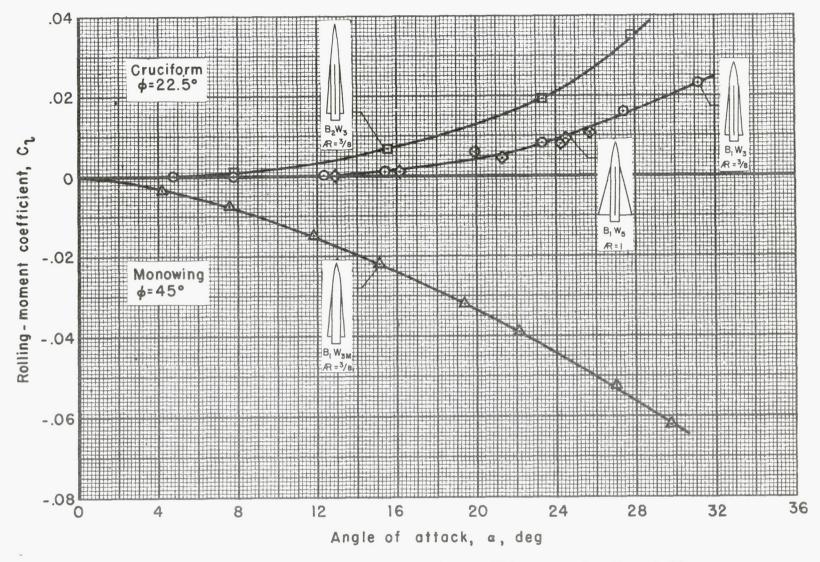
Figure 12.- Effect of arrangement on rolling moments; $M_\infty = 3.33$.

(a) $M_\infty = 1.97$

(b) $M_\infty = 3.33$
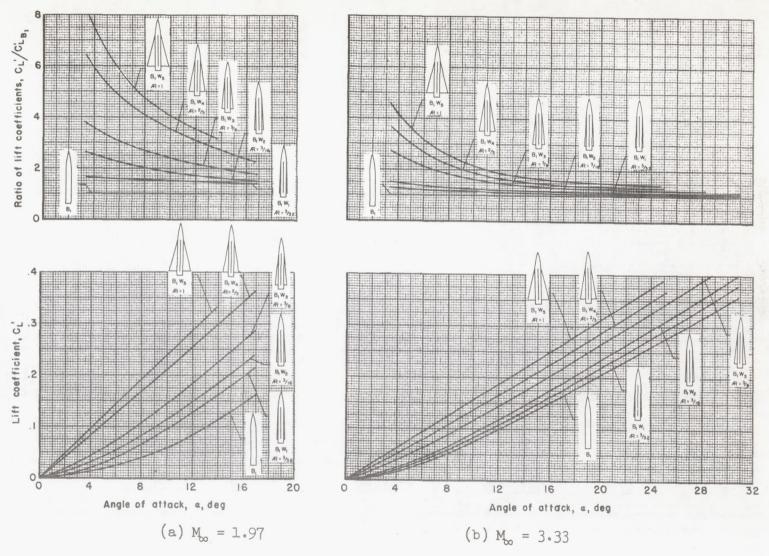
Figure 13.- Comparison of lift effectiveness of winged and wingless missiles.

(a) $M_\infty = 1.97$

(b) $M_\infty = 3.33$
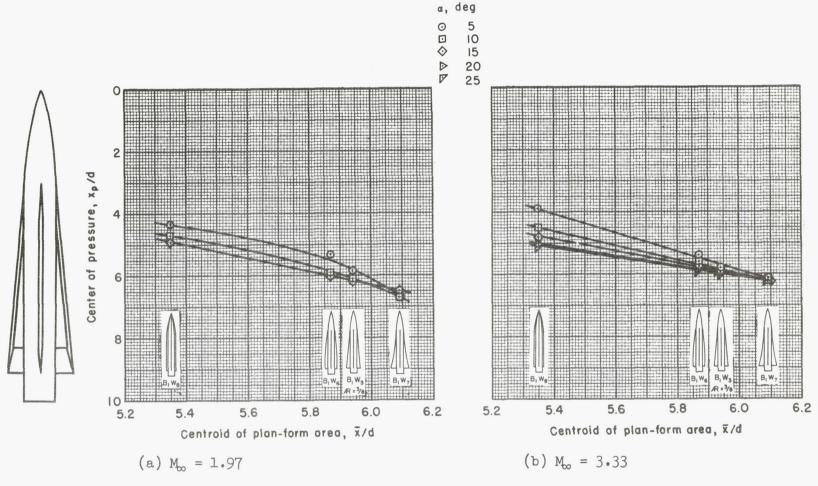
Figure 14.- Variation of center of pressure with centroid of plan-form area for missiles having wings of equal plan-form area.
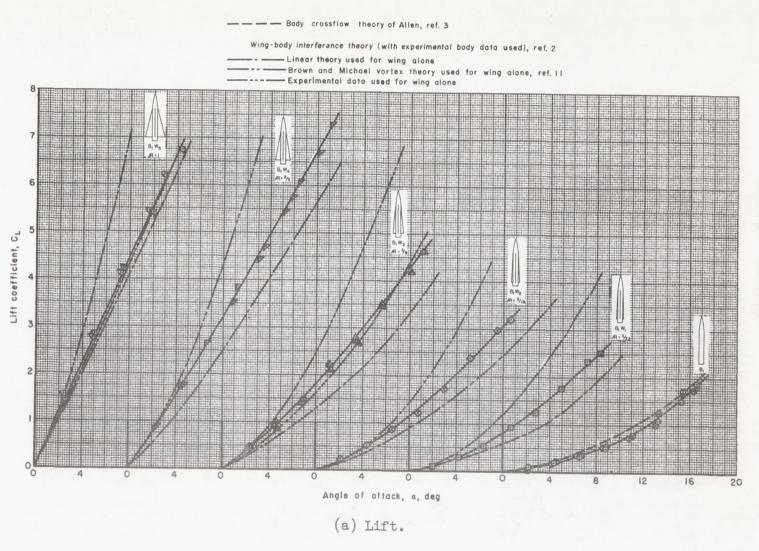
Body crossflow theory of Allen, ref. 3
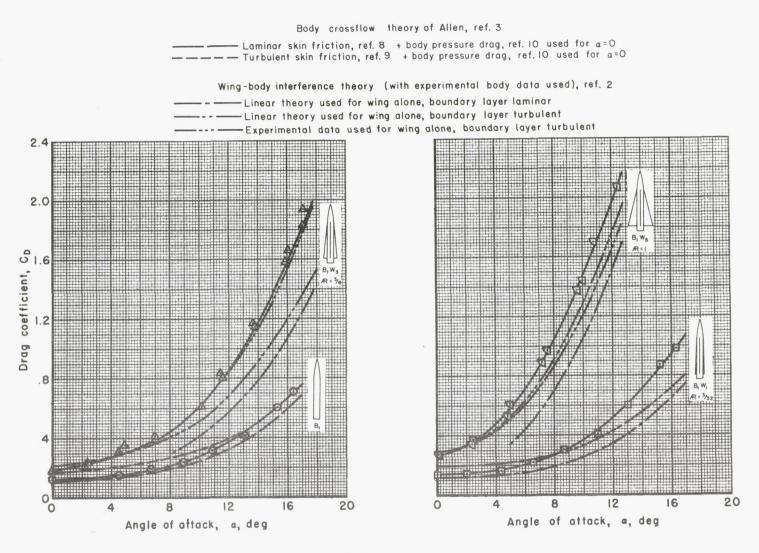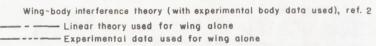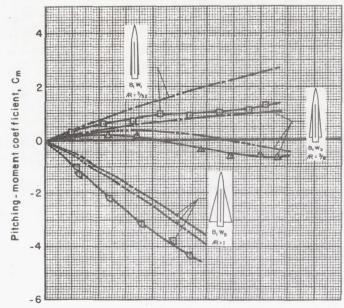
Wing-body interference theory (with experimental body data used), ref. 2
Linear theory used for wing alone
Brown and Michael vortex theory used for wing alone, ref. 11
Experimental data used for wing alone

(a) Lift.

Figure 15.- Comparison of theoretical and experimental aerodynamic characteristics; $M_\infty = 1.97$.

Body crossflow theory of Allen, ref. 3

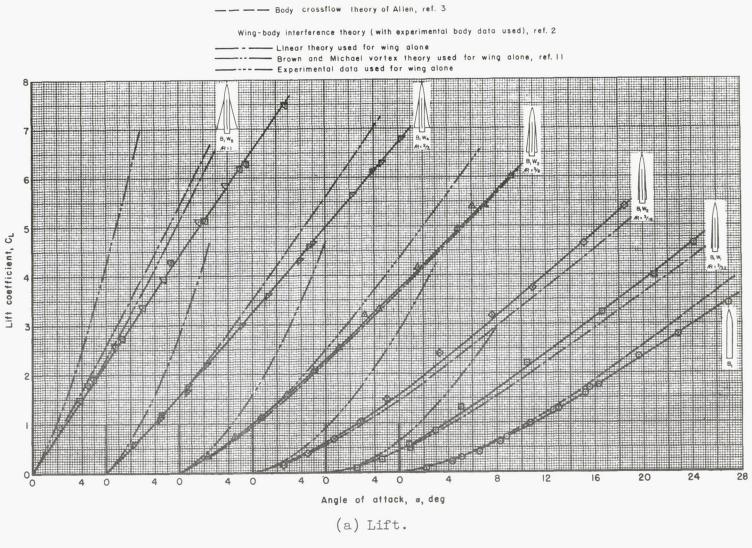——————— Laminar skin friction, ref. 8   + body pressure drag, ref. 10 used for α=0
— — — — — Turbulent skin friction, ref. 9   + body pressure drag, ref. 10 used for α=0

Wing-body interference theory (with experimental body data used), ref. 2

——— – ———Linear theory used for wing alone, boundary layer laminar
——— – · ———Linear theory used for wing alone, boundary layer turbulent
——— – · · ———Experimental data used for wing alone, boundary layer turbulent
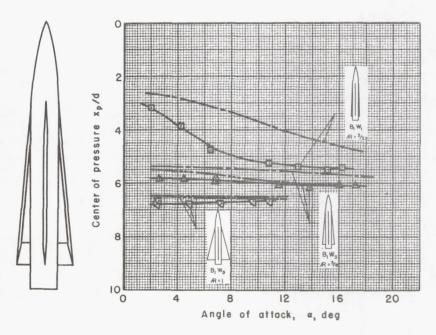
(b) Drag.

Figure 15.- Continued.

Wing-body interference theory (with experimental body data used), ref. 2
——— - ——— Linear theory used for wing alone
——— ---- ——— Experimental data used for wing alone

(c) Pitching moment.

(d) Center of pressure.

Figure 15.- Concluded.

(a) Lift.
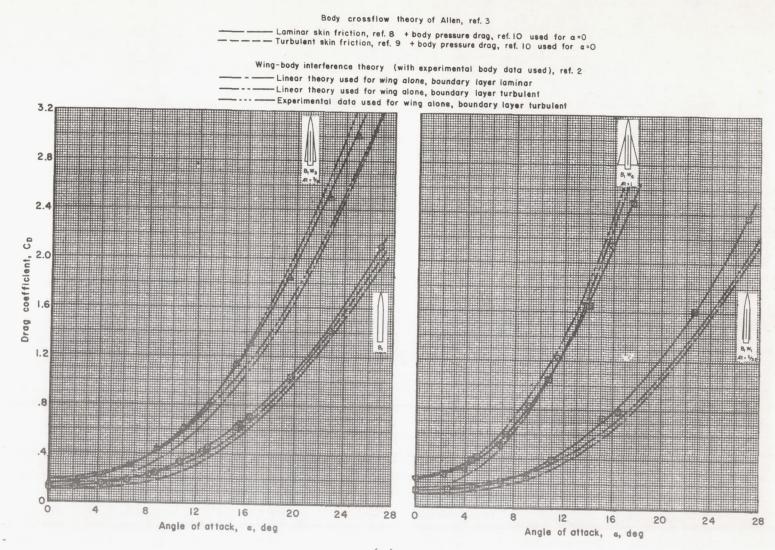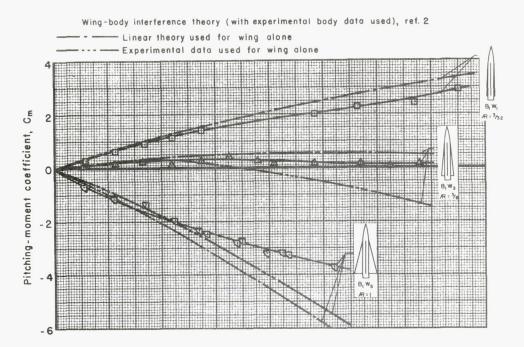
Figure 16.- Comparison of theoretical and experimental aerodynamic characteristics; $M_\infty = 3.33$.

Body crossflow theory of Allen, ref. 3

———————— Laminar skin friction, ref. 8 + body pressure drag, ref. 10 used for $\alpha = 0$
— — — — — Turbulent skin friction, ref. 9 + body pressure drag, ref. 10 used for $\alpha = 0$

Wing-body interference theory (with experimental body data used), ref. 2
— — — Linear theory used for wing alone, boundary layer laminar
—·—·— Linear theory used for wing alone, boundary layer turbulent
—··—··— Experimental data used for wing alone, boundary layer turbulent
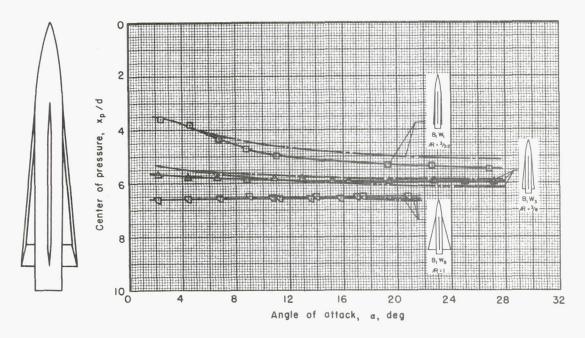
(b) Drag.

Figure 16.- Continued.

Wing-body interference theory (with experimental body data used), ref. 2
Linear theory used for wing alone
Experimental data used for wing alone

(c) Pitching moment.

(d) Center of pressure.

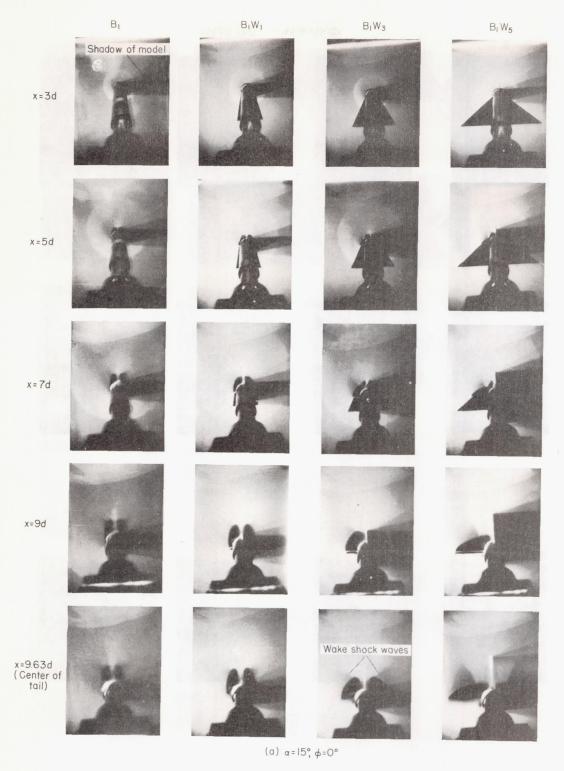Figure 16.- Concluded.

(a) $\alpha = 15°$, $\phi = 0°$
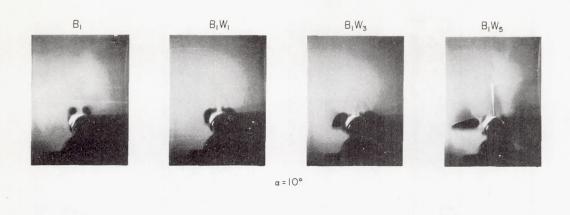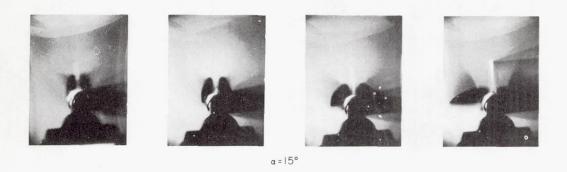
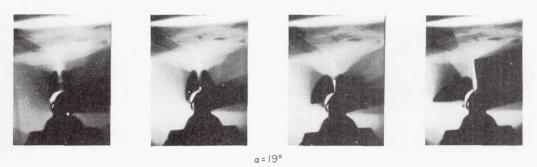Figure 17.— Vapor-screen photographs of models at Mach number 3.3.

B₁   B₁W₁   B₁W₃   B₁W₅

$\alpha = 10°$

$\alpha = 15°$

$\alpha = 19°$

(b) x = 9.63 d (Center of tail),
$\phi = 0°$
Figure 17.— Continued.

$\phi=0°$ $\phi=-22.5°$ $\phi=-45°$ $\phi=0°$ $\phi=-22.5°$ $\phi=-45°$

x=3d

x=7d

x=9.63d
(Center of
tail)

(c) B_1W_{5M}
$\alpha=15°$

(d) B_1W_{5M}
$\alpha=19°$

Figure 17.— Concluded.

Top view

Side view

Vortex trace

Separation region

(a) B_1
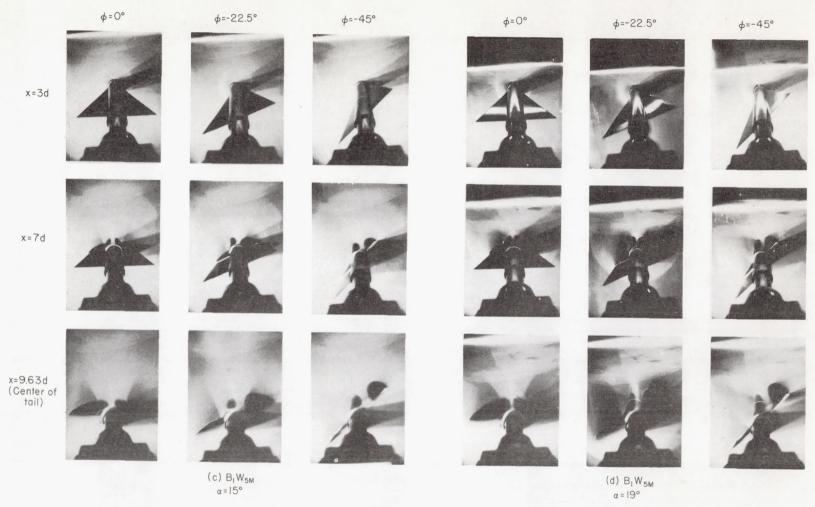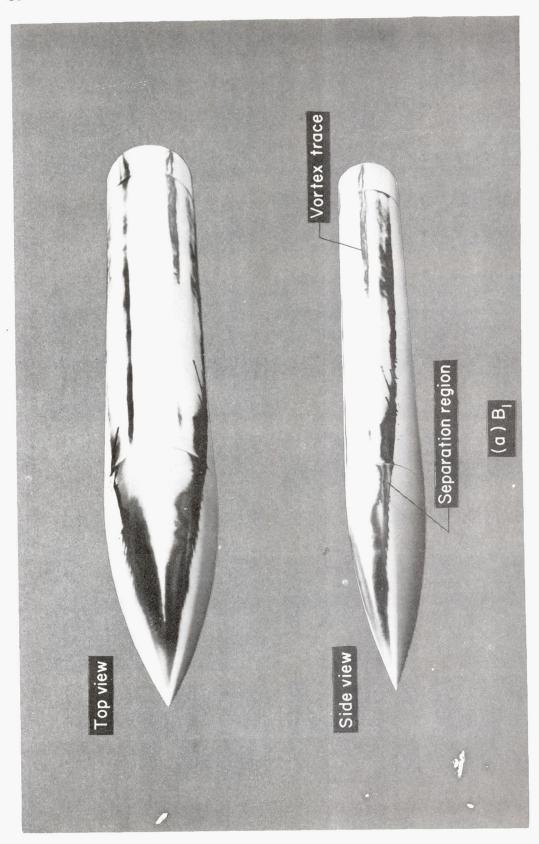
Figure 18.- China-clay photographs of models at Mach number 3.3; $a=15°$, $\phi=0°$.

Top view

Side view

Bottom view

(b) $B_1 W_3$

Figure 18.- Continued.

Top view

Side view

Bottom view

(c) $B_1 W_5$

Figure 18.- Concluded.